NJC

ROYAL SOCIETY OF CHEMISTRY

COMMUNICATION

View Article Online
View Journal | View Issue

Cite this: *New J. Chem.*, 2024, **48**, 1071

Received 4th October 2023,
Accepted 7th December 2023

DOI: 10.1039/d3nj04635d

rsc.li/njc

Hydrothermal conversion of cerium oxalate to CeO_2: a parade of oxalate and water coordination modes†

Navid Assi,[a] Christophe Lahoud,[b] Petr Brázda,[c] Dominika Zákutná,[a] Daniel N. Rainer,[d] Jakub Hraníček,[e] Jan Rohlíček[c] and Václav Tyrpekl *[a]

Hydrothemal conversion of lanthanide/actinide oxalate salts to nanocrystalline oxide has gained technological importance in the chemistry of *f*-elements. Herein, we present a study describing the mechanism behind the hydrothermal recrystallization and decomposition of cerium (and Ce-Gd) oxalate to oxide. Structural determination of all intermediate nanocrystalline products was possible thanks to three-dimensional electron diffraction. This work reveals the enormous structural abilities of simple oxalate ligands.

Oxalates are low-cost, simple, but essential species in the chemistry of transition metals, lanthanides,[1] and actinides.[2] Thanks to the low solubility of oxalate salts, oxalic acid is used: as a separation agent of metal ions from aqueous solutions; as a ligand in coordination compounds; in metal–organic frameworks. These salts can be converted readily to nano- and microcrystalline oxides by an appropriate calcination cycle, typically beyond 600 °C.[3,4] Recently, Walter *et al.*[5] reported the conversion of uranium(IV) oxalates to oxide under hydrothermal conditions at mild temperatures (160–250 °C). The authors extended their work on the hydrothermal decomposition of various actinide oxalates (Th, U, Np, Pu)[6] and their solid solutions.[7,8] Typically, an oxalate dispersion in pure water (pH adjusted or in the presence of hydrazine) is loaded into an autoclave and treated at 100–250 °C. This procedure results in agglomerates of AnO_2 nanoparticles of approximate size 3 to 10 nm. Later, comprehensive studies were conducted by Manaud *et al.* on Th(IV)[9] and U(IV)[10] while changing the main reaction parameters (pH, temperature, and time). There was a clear link between the treatment temperature, pH of the solution, and the crystallite size and morphology of the final product. Recently, Baumann *et al.*[11] compared the hydrothermal and thermal conversion of Pu(IV) oxalate to nanocrystalline PuO_2 mentioning most of the positive aspects of the hydrothermal route: lower temperature, shorter reaction time, and lower content of residual carbon. All the above-mentioned works described a drastic change in the morphology of the starting powder during the process. However, tracking of the reaction mechanism is complicated due to the hydrothermal conditions, so determination of the structure of intermediates is complicated due to nanocrystallinity. Therefore, the detailed reaction mechanisms are not known. Few studies have described the hydrothermal treatment of cerium oxalate. Flower-like CeO_2 microcrystals were hydrothermally synthesized from an oxalate precursor in an alkaline environment and hydrogen peroxide.[11] A similar procedure yielding hierarchical mesoporous ceria was obtained in the presence of some amino acids previously.[12] Recently, mixed $U_{1-x}Ce_xO_{2+\delta}\cdot nH_2O$ ($0.1 \leq x \leq 0.7$) solid solutions were prepared using this method.[13]

Herein, we focused on the hydrothermal conversion of pure cerium oxalate hydrate to oxide. Ceria has been in the spotlight for many decades, mainly due to its applicability in fuel cells,[14] catalysis,[15] and Pu surrogates.[16] The mechanism of the decomposition and recrystallisation of oxalate (which is responsible for such a drastic change in the morphology of the agglomerates) was studied in detail. This was possible thanks to the newly developed technique of three-dimensional electron diffraction (3D ED), which enabled complete determination of the structure without the need for large crystals.[17–22] In addition, we tested the ability of this route to convert mixed $Ce_{1-x}Gd_x(C_2O_4)_3\cdot 10H_2O$ solid solutions to $Ce_{1-x}Gd_xO_{2-x/2}$ (x = 0.1, 0.2, 0.3).

[a] *Department of Inorganic Chemistry, Faculty of Science, Charles University, Hlavova, 2030/8, Prague 12800, Czech Republic. E-mail: vaclav.tyrpekl@natur.cuni.cz*
[b] *Université Aix-Marseille, Faculty of Science, Site St. Jérôme, 52 Avenue Escadrille Normandie Niemen, Marseille 13013, France*
[c] *Department of Structure Analysis, Institute of Physics of the Czech Academy of Sciences, Prague 18221, Czech Republic*
[d] *Department of Physical and Macromolecular Chemistry, Faculty of Science, Charles University, Hlavova, 2030/8, Prague 12800, Czech Republic*
[e] *Department of Analytical Chemistry, Faculty of Science, Charles University, Hlavova, 2030/8, Prague 12800, Czech Republic*

† Electronic supplementary information (ESI) available. CCDC 2296196–2296199. For ESI and crystallographic data in CIF or other electronic format see DOI: https://doi.org/10.1039/d3nj04635d

Pure and mixed oxalates were prepared by heterogeneous precipitation as detailed previously[1,23] (a description is in the ESI†). Briefly, for the hydrothermal conversion, 250 mg (0.35 mmol) of $Ce_2(C_2O_4)_3{\cdot}10H_2O$ or $Ce_{1-x}Gd_x(C_2O_4)_3{\cdot}10H_2O$ (x = 0.1, 0.2, 0.3) was placed in a Teflon™-lined autoclave (capacity of 50 mL) together with distilled water (21 mL) or nitric acid solution of the desired pH. Solutions of $HClO_4$ and HCl, as nonoxidizing acids, were also tested instead of HNO_3. The mixture was treated at 180–220 °C for ≥ 24 h. The final product was purified by repeated centrifugation and dried at 50 °C under air. All prepared materials were analysed by powder X-ray diffraction (PXRD), scanning electron microscopy (SEM), transmission electron microscopy (TEM), and thermogravimetric analysis (TGA). The sample was treated in pure water (pH = 7, 220 °C, 48 h) and analysed using 3D ED. A detailed description of the analytical techniques is given in the ESI.†

$Ce_2(C_2O_4)_3{\cdot}10H_2O$ can be converted completely to oxide in aqueous nitric acid solution (pH = 1) at >180 °C. Optimal conditions were found to be 24 h and 220 °C to yield a powder of grain size 200–500 nm (Fig. 1). The final size of CeO_2 crystals increased with the applied temperature (see the micrographs in Fig. S1 and infrared spectra in Fig. S2, ESI†).

A short study of the hydrothermal conversion of $Ce_{1-x}Gd_x(C_2O_4)_3{\cdot}10H_2O$ (x = 0.1, 0.2, 0.3) solid solutions showed that the conditions mentioned above (HNO_3 solution, pH = 1) were valid for mixed oxides giving homogeneous nanocrystalline $Ce_{1-x}Gd_xO_{2-x/2}$ (see Fig. S3 and S4 and PXRD in Fig. S5, ESI†). However, the yield of Gd(III) incorporation in CeO_2 was not quantitative and showed some fluctuations (see ICP-MS analyses in Table S1, ESI†). Further studies in this direction are beyond the scope of the current work.

The presence of an oxidizing acid (HNO_3) solution was of paramount importance. It facilitated the oxidation of Ce(III) ions to Ce(IV) ions, leading to the oxide. Hydrothermal conversion in HCl or $HClO_4$ (non-oxidizing acids) solutions of pH = 1 did not lead to CeO_2 (see the XRD results of samples obtained after 24 h at 220 °C in Fig. S6, ESI†). Different concentrations of nitric acid (pH = 1 to 7) in the autoclave batch led to different degrees of conversion. Fig. 2 shows $Ce_2(C_2O_4)_3{\cdot}10H_2O$ treated in solutions of pH 1 to 7 (HNO_3). In pure water (pH = 7), recrystallisation and a drastic change in morphology occurred, but decomposition to CeO_2 was not reached (Fig. 2, top and middle row). The original cerium oxalate with a flat needle morphology (Fig. S6, ESI†) changed to large rods (from 10 × 10 × 100 μm and larger) with well-developed crystal facets parallel to the elongation direction. Increasing the concentration of nitric acid led to the decomposition of the recrystallized material to oxide (Fig. 2, bottom row). This process was accompanied by full disintegration of the rods to nanocrystals, which sometimes remained assembled to the initial rod shape. A change in agglomerate morphology has been described for all hydrothermally converted oxalates.[5–10] This is one of the main differences with thermal conversion, during which the initial oxalate shape is retained.[1,3,23,24]

Recrystallisation was also studied from the crystallographic viewpoint. The PXRD patterns of selected samples were plotted (Fig. 3). Unfortunately, structure matching from PXRD was possible only for the initial cerium oxalate and final cerium dioxide. Tracking the intermediate phases and resolving their structures was difficult due to the nanocrystallinity of the material and the coexistence of several phases in the samples.

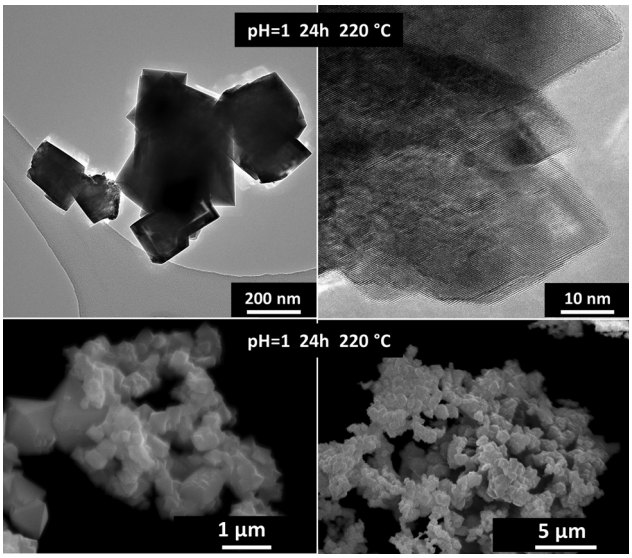

Fig. 1 Transmission (top) and scanning (bottom) electron micrographs of CeO_2 powder obtained by the hydrothermal decomposition of $Ce_2(C_2O_4)_3{\cdot}10H_2O$ in nitric acid solution (pH = 1) at 220 °C for 24 h.

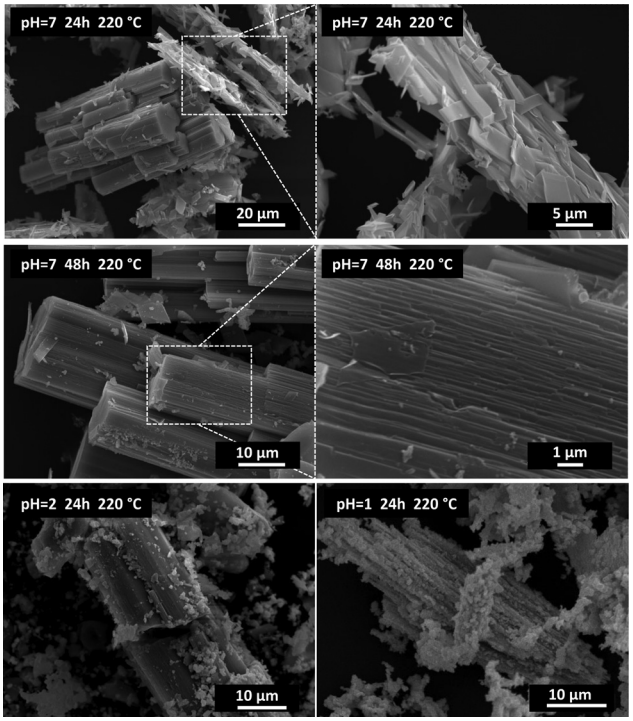

Fig. 2 Scanning electron micrographs of cerium oxalate with different degrees of conversion to CeO_2. Assemblies of the recrystallised phase with initial $Ce_2(C_2O_4)_3{\cdot}10H_2O$ (top), recrystallisation and change of morphology to rods (middle), and disintegration of the rods to nanocrystalline CeO_2 (bottom).

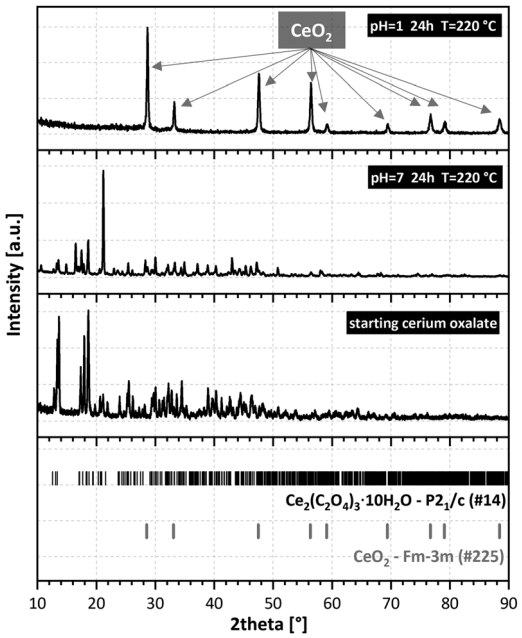

Fig. 3 Powder X-ray diffraction of the initial $Ce_2(C_2O_4)_3{\cdot}10H_2O$ (bottom), hydrothermally treated (middle), and final CeO_2 (top).

This was overcome thanks to 3D ED enabling structural determination of small, unstable, or problematic crystals unsuitable for single-crystal XRD. The structure of the initial oxalate is well known. It crystallizes in the $P2_1/c$ space group with four Ce(III) ions in the elementary cell, each bonded to three oxalate groups and three water molecules in the primary coordination sphere.[25] Two additional water molecules are present in each of the four cavities formed by the oxalate coordination polymer. Therefore, the molecular formula should be written as $Ce_2(C_2O_4)_3(H_2O)_6{\cdot}4H_2O$, as for some An(III) oxalates with a similar structure.[26] There are two formula units within the elementary cell. The recrystallized sample at 220 °C (pH = 7, 24 and 48 h) was selected for structural analysis by 3D ED. This sample showed full recrystallization of the oxalate but low decomposition to oxide (Fig. 3). In total, 114 datasets were indexed. Except for the known initial decahydrate structure (42 indexed datasets), four other structures were observed (72 indexed datasets in total), as shown in Table 1 (full information is given in Table S2, ESI†). The structures were all solved *ab initio* by the Superflip program.[27] The structure present in most of the transformed oxalate hydrates was the orthorhombic $P2_12_12_1$ of $Ce_2(C_2O_4)_3(H_2O)_4$. Isostructural Pr and Nd oxalates have been described in the ICSD database.[28,29] The other three structures have not been reported.

The second most abundant phase was a structure with triclinic $P\bar{1}$ symmetry. If all the water molecules were fully occupied, then the structure was pentahydrate $Ce_2(C_2O_4)_3(H_2O)_4{\cdot}H_2O$ (see the detailed discussion of the level of hydration in the ESI†). Four water molecules in the formula unit were coordinated to cerium ions and the fifth one resided in a pore. Two other phases, orthorhombic *Pbcn* and monoclinic $P2_1/n$, were significantly less abundant and much more disordered judging from the observed diffuse scattering. Both phases were pentahydrate, with four water molecules coordinated to two independent cerium atoms. The fifth water molecule was in a cavity. Hydrolysis or formation of hydroxo-complexes were not observed until the final oxalate decomposition. Probably a higher pH would be required to observe such behavior, as has been observed with Nd.[30] The results of 3D ED were supported by PXRD Rietveld analysis of the sample treated at 220 °C for 48 h (Fig. S7, ESI†). The best fit was obtained using the $P2_12_12_1$ and $P\bar{1}$ phases having the highest abundance in the sample.

Evidently, the four structures had common structural motives worth mentioning. In all structures, oxalate ions adopted bridging coordination modes (Fig. S8, ESI†) to connect cerium ions with coordination modes 1 : 2, 1 : 2 + 1 and 1 : 2 + 2 (Fig. S8, top from left, ESI†), extending the list of oxalate coordination modes for rare-earth ions.[31] The oxalates in the $P2_12_12_1$ structure formed infinite chains along two nearly perpendicular directions, which created a ''wine rack'' structural motif (Fig. 4, left). Higher coordination numbers in the *Pbcn*, $P\bar{1}$ and $P2_1/n$ structures were probably caused by a specific organization of the infinite chains of oxalates with the 1 : 2 coordination mode solely, all aligned in the same direction. Layers of oxalates with higher denticity were then perpendicular to these polymer chains (Fig. 4, right), here 1 : 2 and 1 : 2 + 2 modes were present.

Six cerium coordination polyhedra were found in the four structures. Type 1 comprised the cerium ion coordinated by nine ligands. Two water molecules were in the *cis* conformation, with one monodentate oxalate and three bidentate oxalates (Fig. S9, ESI†). Types 2, 3, and 4 are shown in Fig. S10 (ESI†). Coordination was achieved by 10 ligands, two water molecules in *trans* positions, and two oxalates in the perpendicular direction forming infinite chains. There were two bidentate oxalates in the other perpendicular direction. Type 5 revealed sole coordination by five oxalates (nine oxalate oxygens (Fig. S11, ESI†)), four bidentates and one monodentate. Type 6 involved non-participation in the infinite chains and, except for three bidentate oxalates, it was coordinated to four water molecules (Fig. S12, ESI†). For more details, see the ESI.†

Table 1 Crystallographic details of hydrothermally recrystallized cerium oxalate phases

Stoichiometric formula	$Ce_2(C_2O_4)_3(H_2O)_4$	$Ce_2(C_2O_4)_3(H_2O)_4{\cdot}H_2O$	$Ce_2(C_2O_4)_3(H_2O)_4{\cdot}H_2O$	$Ce_2(C_2O_4)_3(H_2O)_4{\cdot}H_2O$
Occurrence (% of cases)	40	39	14	7
Crystal system	Orthorhombic	Triclinic	Orthorhombic	Monoclinic
Space group	$P2_12_12_1$	$P\bar{1}$	*Pbcn*	$P2_1/n$
a, b, c (Å)	8.64(1), 9.59(1), 16.87(1)	10.50(1), 11.77(1), 12.97(1)	22.06(8), 12.96(1), 10.61(1)	21.67(1), 10.51(1), 12.97(1)
α, β, γ (°)	90, 90, 90	92.91(4), 90.58(4), 112.95(4)	90, 90, 90	90, 93.58(4), 90
Z	4	4	8	8

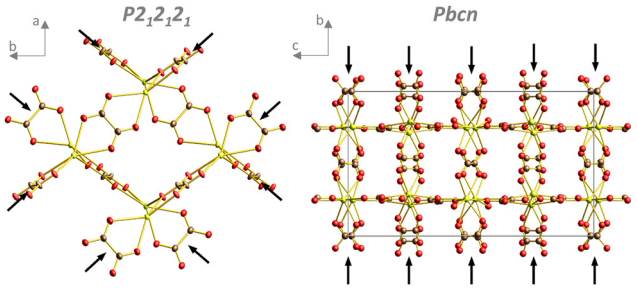

Fig. 4 Oxalates in the $P2_12_12_1$ structure form infinite chains running along two nearly perpendicular directions (black arrows; the other oxalate molecule and coordinated water molecules have been omitted for clarity). *Pbcn* structure with infinite oxalate chains running only along one direction marked by black arrows (coordinated water molecules and water in pores have been omitted for clarity).

As mentioned above, in the *Pbcn*, $P2_1/n$, and $P\bar{1}$ structures, there were oxalate layers perpendicular to the direction of the infinite oxalate chains. The structural motifs in these layers were almost identical for *Pbcn* and $P2_1/n$ phases (Fig. 5, left and middle). The difference was that four water molecules were in the layer in the *Pbcn* structure, but an oxalate replaced it in the $P2_1/n$ phase. The four coordinated molecules in *Pbcn* pointed outwards from the layer in the direction of the infinite oxalate chains and were coordinated to one cerium atom (type 4). In the $P\bar{1}$ structure, the layer motif was slightly simpler (Fig. 5, right).

The global water content in the sample treated at 220 °C for 24 h was measured by thermogravimetry, and $Ce_2(C_2O_4)_3 \cdot 3.5H_2O$ is shown in Fig. S13 (ESI†). From the crystallographic analysis considering two main phases, the composition was estimated to be $Ce_2(C_2O_4)_3 \cdot 4.5H_2O$ (*i.e.*, one water molecule more than determined by thermogravimetry). This was probably caused by lower occupancy of water molecules coordinated to cerium (type 4) and those within the pores (deeper discussion is provided in the ESI†).

Similar to that in,[32,33] hydrothermal crystallization was typically not a single-step process. Here, we reported the mechanism of hydrothermal conversion of $Ce_2(C_2O_4)_3 \cdot 10H_2O$ to oxide. The whole mechanism is expressed graphically in Fig. 6.

Hydrothermal dehydration and recrystallisation of oxalate take place prior to the conversion to oxide, which is responsible for the enormous change in morphology during this process. 3D ED was crucial for structural determination of nanocrystalline samples. The loss of water was linked with an increase in

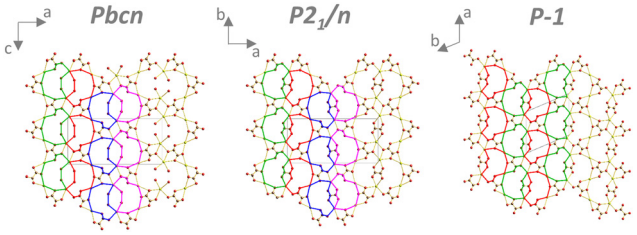

Fig. 5 Structural motifs of oxalate layers perpendicular to the infinite coordination polymer chains. Coordinated water molecules (except those forming the oxalate layer and water in pores) have been omitted for clarity.

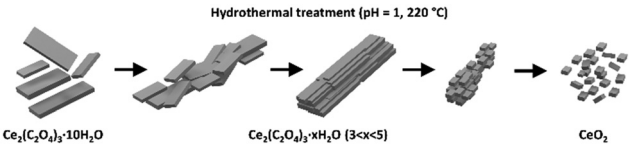

Fig. 6 Graphical illustration of the mechanism of hydrothermal conversion of $Ce_2(C_2O_4)_3 \cdot 10H_2O$ to CeO_2.

the denticity and coordination mode of the oxalate ligand, and elicited several structurally analogous phases. The change in the oxidation state of cerium, together with oxalate decomposition, seemed to be the final one-step process visible as a disintegration of the recrystallised phases to oxide. In addition to structural investigations, we tested the possibility of hydrothermal conversion of Ce-Gd oxalates to mixed oxides.

Conflicts of interest

There are no conflicts of interest to declare.

Acknowledgements

This study was funded by the Czech Science Foundation (GAČR) (project 20-20936Y). P.B. and J. R. acknowledge GAČR (project 21-05926X), the CzechNanoLab Research Infrastructure (MEYS CR, LM2018110) and the Operational Programme Research, Development and Education by the EU ESIF and MEYS CR (SOLID21 CZ.02.1.01/0.0/0.0/16_019/0000760).

Notes and references

1 A. Alemayehu, D. Zákutná, S. Kohúteková and V. Tyrpekl, *J. Am. Ceram. Soc.*, 2022, **105**, 4621.
2 F. Abraham, B. Arab-Chapelet, M. Rivenet, C. Tamain and S. Grandjean, *Coord. Chem. Rev.*, 2014, **266–267**, 28.
3 V. Tyrpekl, J.-F. Vigier, D. Manara, T. Wiss, O. Dieste Blanco and J. Somers, Low temperature decomposition of U(IV) and Th(IV) oxalates to nanograined oxide powders, *J. Nucl. Mater*, 2015, **460**, 200.
4 L. De Almeida, S. Grandjean, N. Vigier and F. Patisson, *Eur. J. Inorg. Chem.*, 2012, 4986.
5 O. Walter, K. Popa and O. Dieste Blanco, *Open Chem.*, 2016, **14**, 170.
6 K. Popa, O. Walter, O. Dieste Blanco, A. Guiot, D. Bouëxière, J. Y. Colle, L. Martel, M. Naji and D. Manara, *CrystEngComm*, 2018, **20**, 4614.
7 L. Balice, D. Bouëxière, M. Cologna, A. Cambriani, J. F. Vigier, E. De Bona, G. D. Sorarù, C. Kübel, O. Walter and K. Popa, *J. Nucl. Mater.*, 2018, **498**, 307.
8 V. Baumann, K. Popa, O. Walter, M. Rivenet, G. Senentz, B. Morel and R. J. M. Konings, *Nanomaterials*, 2023, **13**, 340.
9 J. Manaud, J. Maynadié, A. Mesbah, M. O. J. Y. Hunault, P. M. Martin, M. Zunino, N. Dacheux and N. Clavier, *Inorg. Chem.*, 2020, **59**, 14954.

10 J. Manaud, J. Maynadié, A. Mesbah, M. O. J. Y. Hunault, P. M. Martin, M. Zunino, D. Meyer, N. Dacheux and N. Clavier, *Inorg. Chem.*, 2020, **59**, 3260.
11 W. Liu, L. Feng, C. Zhang, H. Yang, J. Guo, X. Liu, X. Zhang and Y. Yang, *J. Mater. Chem. A*, 2013, **1**, 6942.
12 G. Zhang, Z. Shen, M. Liu, C. Guo, P. Sun., Z. Yuan, B. Li, D. Ding and T. Chen, *J. Phys. Chem. B*, 2006, **110**, 25782.
13 S. Benarib, N. Dacheux, X. F. Le Goff, J. Lautru, L. Di Mascio and N. Clavier, *Dalton Trans.*, 2023, **52**, 10951–10968.
14 H. Inaba and H. Tagawa, *Solid State Ionics*, 1996, **83**, 1.
15 T. Montini, M. Melchionna, M. Monai and P. Fornasiero, *Chem. Rev.*, 2016, **116**, 5987.
16 K. Choi, W. Tong, R. D. Maiani, D. E. Burkes and Z. A. Munir, *J. Nucl. Mater.*, 2010, **404**, 210.
17 L. Palatinus, P. Brázda, M. Jelínek, J. Hrdá, G. Steciuk and M. Klementová, *Acta Crystallogr., Sect. B: Struct. Sci., Cryst. Eng. Mater.*, 2019, **75**, 512.
18 P. Brázda, L. Palatinus and M. Babor, *Science*, 2019, **364**, 667.
19 P. Brázda, M. Klementová, Y. Krysiak and L. Palatinus, *IUCrJ*, 2022, **9**, 735.
20 P. B. Klar, Y. Krysiak, H. Xu, G. Steciuk, J. Cho, X. Zou and L. Palatinus, *Nat. Chem.*, 2023, **15**, 848–855.
21 L. Palatinus, V. Petříček and C. A. Correa, *Acta Crystallogr., Sect. B: Struct. Sci., Cryst. Eng. Mater.*, 2015, **A71**, 235.
22 V. Petříček, L. Palatinus, J. Plášil and M. Dušek, *Z. Kristallogr.*, 2023, **238**, 271.
23 V. Tyrpekl, P. Markova, M. Dopita, P. Brázda and M. A. Vacca, *Inorg. Chem.*, 2019, **58**, 10111.
24 R. Podor, N. Clavier, J. Ravaux, L. Claperde and N. Dacheux, *J. Amer. Ceram. Soc.*, 2012, **95**, 3683.
25 Dicerium trioxalate decahydrate, ICSD: 109637, Inorganic Crystal Structure Database, **https://www2.fiz-karlsruhe.de/icsd_home.html**, January 2018.
26 C. Tamain, B. Arab-Chapelet, M. Rivenet., X. F. Legoff, G. Loubert, S. Grandjean and F. Abraham, *Inorg. Chem.*, 2016, **55**, 51.
27 L. Palatinus and G. Chapuis, *J. Appl. Crystallogr.*, 2007, **40**, 786.
28 J. C. Trombe and J. Jaud, *J. Chem. Crystallogr.*, 2003, **33**, 19.
29 C. J. Hao and H. Xie, *Acta Cryst.*, 2012, **E68**, m444.
30 A. Mer, M. Rivenet, L. De Almeida, S. Granjean and F. Abraham, *Inorg. Chem. Commun.*, 2013, **31**, 90.
31 M. Hernández-Molina, P. A. Lorenzo-Luis and C. Ruiz-Pérez, *CrystEngComm*, 2001, **16**, 1.
32 L. Wang, R. Zhao, C. Wang, L. Yuan, Z. Gu., C. Xiao, S. Wang, X. Wang, Y. Zhao, Z. Chai and W. Shi, *Chem. – Eur. J.*, 2014, **20**, 12655.
33 L. Wang, R. Zhao, X. Wang, L. Mei, L. Yuan, S. Wang, Z. Chai and W. Shi, *CrystEngComm*, 2014, **16**, 10469.